scientific reports

Check for updates

OPEN

Transmission energy dispersive X-ray diffraction as a tool for the laboratory study of fast processes in metals

Daniel Vavrik[1,4✉], Vjaceslav Georgiev[2], Jan Jakubek[3], Bohuslav Masek[5], Ondrej Urban[2], Jan Sleichrt[1] & Daniel Kytyr[1]

In this work, an in-situ study of phase transitions in low-carbon steel is presented. The phase changes were monitored by the transmission energy dispersive X-ray diffraction technique during the heating, annealing and quenching cycle of the sample under standard laboratory conditions. During energy dispersive X-ray diffraction, the sample volume was transmitted with a pencil beam generated by a standard polychromatic X-ray tube without any spectral filtering. Two-dimensional polychromatic diffraction images were acquired by a Timepix 3 pixelated detector. This detector is capable of achieving a throughput of up to 38 Mhits/s in continuous stream mode using USB 3.0 interface. For each detected photon, its position is known with an accuracy of 55 μm in the detector plane and its energy with a resolution of 4 keV at 60 keV. The recorded polychromatic data is then recomputed to get the equivalent monochromatic XRD pattern that would be produced using a monochromatic X-ray source. Thanks to the 90 kV voltage potential of the X-ray tube, the polychromatic pencil beam was able to pass through a highly attenuating sample made of 1.5 thick steel sheet. In addition, by utilizing the entire X-ray spectrum, the pencil beam has a sufficiently high brilliance to obtain XRD patterns rapidly enough to investigate relatively fast processes with temporal resolution of 10 s. It made to possible to analyze the phase transitions in a polycrystalline sample during its temperature treatment under standard laboratory conditions.

In all areas of industry, there is a constant demand for products with complex shapes and the best possible mechanical properties at a low price. One of the ways to achieve this goal and to meet the demanding requirements of designers is the use of high-strength, low-alloy steels processed by advanced heat treatment procedures. Related advanced high-strength steels (AHSS)[1] and ultra-high strength steels (UHSS)[2] have very complex and hierarchical microstructures made up of ferrite, austenite, bainite, and a martensite matrix, as well as duplex or multiphase mixes of these elements supplemented with precipitates. Thanks to the excellent properties of high-strength steels, the possibilities of their use are continuously growing, while new technologies are being sought to further improve their mechanical properties. One of the procedures is Quenching and Partitioning (Q-P)[3], which is closely related to processes using the partial clouding of steel with a subsequent redistribution of carbon, and it represents one of the modern methods of the heat treatment of high-strength steels. The resultant mechanical properties of steel treated by the Q-P procedure depend on the heat-treatment profile[3], where possibly applied mechanical loading may play a role[4]. It is therefore highly desirable to test various heat-treatment profiles, possibly accompanied by mechanical loading, on the resulting microstructure of the steel under investigation. Obviously, such experimental work must be carried out on a bulk sample during the process under investigation, and the sample should be of sufficient thickness/volume to ensure that the internal temperature is approximately uniform during the test, even if an unavoidable temperature gradient appears on the surface of the sample. In order to understand the processes occurring during heat treatment, it is of course necessary to observe the kinematics of the phase changes in the steel. The well-established X-ray diffraction method is routinely used to characterize crystalline materials. In this work, a newly developed laboratory variant of the XRD system was used. The main objective of this development was to provide the ability to test a

[1]Institute of Theoretical and Applied Mechanics, Czech Academy of Sciences, Prosecka 809/76, 190 00 Prague, Czech Republic. [2]Faculty of Electrical Engineering, University of West Bohemia, Univerzitni 2795/26, 301 00 Pilsen, Czech Republic. [3]Advacam, U Pergamenky 12, 170 00 Prague, Czech Republic. [4]Institute of Experimental and Applied Physics, Czech Technical University in Prague, Husova 5, 110 00 Prague, Czech Republic. [5]COMTES FHT a.s, Dobřany, Czech Republic. ✉email: vavrik@itam.cas.cz

1

wide range of samples with sufficient temporal resolution during different heat-treatment temperature profiles, possibly with external mechanical loading.

The problem of the time-resolved study of phase transformation within bulk material has been successfully solved in recent years by the high energy X-ray diffraction (HEXRD) method[3–10]. HEXRD, based on high energy (>80 keV) and intensive monochromatic synchrotron radiation, enables the transmission of bulk samples, while the time resolution ranges from seconds[5] to tenths of a second[6] depending on the synchrotron X-ray source used and the material tested. If material under study is homogeneous and isotropic, the diffraction pattern recorded by the 2D detector has the form of the concentric circles—Debye Scherrer (DS) rings. While each ring related to the specific diffraction angle corresponds to the specific crystalline lattice plane—lattice parameters can be measured this way. And, where appropriate, the relative proportions of the constituents of complex materials can be derived by analyzing the diffraction pattern[6,7]. DS rings themselves are formed from huge amounts of reflection spots caused by individual crystals. When a polycrystalline material is texture free, the intensity along DS rings is constant. On other hand, texture causes variations of the intensity along the DS rings, and the diffracted intensity originates from different texture components[5,6]. If some tensile strain is present, DS circles are changed into ellipses; the local lattice strain–stress tensor can be derived on this basis[8–10]. Increasing temperature causes expansion of the DS rings, as it allows studying the related dependence of the lattice parameters on temperature[7]. In addition, a detailed analysis of DS rings allows studying the evolution of steel fractions during heat treatment (occurrence/disappearance of the DS rings)[8,10]. In the case of a limited number of crystals in the sample and a high-resolution 2D detector, it is possible to reconstruct the 3D structure of crystalline materials using the principles of computed tomography, where the shapes and orientations of single crystals are obtained. For this purpose, diffraction patterns and images of X-ray attenuation during sample rotation are recorded. A related technique is known as HEXRD microscopy[11].

In general, not only for HEXRD, if no strain or preferred orientation is present a radial or circular integration can be carried out to give a 1D diffraction pattern. It allows reduction of the measurement time and/or improvement in the temporal resolution in relation to the kinetics of the time dependent processes (phase transformation of the steel in our case). However, besides the power of the HEXRD technique, it is not obviously available for routine measurements in daily practice. Therefore, the main objective of this work is to enable the study of phase transformation in bulk material with appropriate temporal resolution under standard laboratory conditions, thus allowing routine measurement on a daily basis to enable routine daily measurements.

Nowadays laboratory X-ray diffractometers have relatively low X-ray beam intensity and limited X-ray photon energy[12]. Therefore, such diffractometers are not appropriate to examine larger bulk samples, especially if a reasonable temporal resolution is needed. Such limitation was overcome by introducing the Energy Dispersive X-Ray Diffraction (EDXRD) technique[13]. This technique uses the whole spectrum of the X-ray tube, including high energies similar to the HEXRD method. Therefore, XRD measurement can be done fast, and even bulk metal samples can be measured in transmission mode in this way. Initially, it was only possible to study 1D diffraction patterns because the necessary energy dispersive detector was only available as a strip detector, see[14] for instance. Relatively recently, the EDXRD method has been enhanced, and new 2D energy dispersive pixel detectors make possible the direct recording and analysis of 2D diffraction patterns. Detectors based on pnCCD technology showed excellent performance for synchrotron diffraction setups[15–18]. While single photon counting detector HEXITEC was used for XRD analysis in[19,20]. Timepix 3 detector[21] used in this work has similar properties. Since this 2D detector have so far approximately one order of magnitude worse energy resolution than conventional detectors, extended data analysis based on Rietveld refinement method[22] is necessary to obtain detailed diffractograms. However, the high efficiency of EDXRD also makes it possible to study relatively fast processes such as heat treatment of steel.

Virtual monochromatization of the polychromatic diffraction pattern utilizing energy dispersive detector

EDXRD technique utilized for investigation of the bulk material is partially similar to the HEXRD method. A collimated high energy X-ray beam transmits the sample, and the diffraction pattern is registered by the planar, energy dispersive detector. A significant difference is that, contrary to HEXRD, the X-ray beam is not monochromatic. A related EDXRD experimental arrangement is depicted in Fig. 1.

The diffractogram produced by a polychromatic source does not have a clear structure, because it is actually a mixture of many diffractograms produced by the entire X-ray beam spectrum. However, such a polychromatic diffractogram can be virtually monochromatized. It can be converted to a monochromatic equivalent like in a standard diffraction method, if information about the energy and diffraction angle of each single photon is known. For such a purpose, an energy-dispersive detector is needed. Although another detector shape would be possible, we are using a Timepix 3 planar detector[16] in our work. Using it, the incident position of each registered photon is known. Therefore, its diffraction and azimuth angle can be calculated as follows, supposing that the pencil beam targets into the detector center (see Fig. 1):

$$X = \left[J - \frac{(j_{max} + 1)}{2} \right] \cdot px - d_x; \; Y = \left[I - \frac{(i_{max} + 1)}{2} \right] \cdot px - d_y \qquad (1)$$

where X and Y are matrixes of the individual pixel x and y coordinates, while the center of the detector is at the orgin of the Cartesian coordinate system. This center can be shifted by the difference $[d_x, d_y]$, if the pencil beam transmitting the specimen doesn't exactly pass the detector center. Matrices I and J represent pixel indexes, while j_{max} and i_{max} denote maximal indexes in the x and y directions, respectively. Also, px is the pixel pitch. Written in matrix form, azimuth angle Φ can be calculated as:
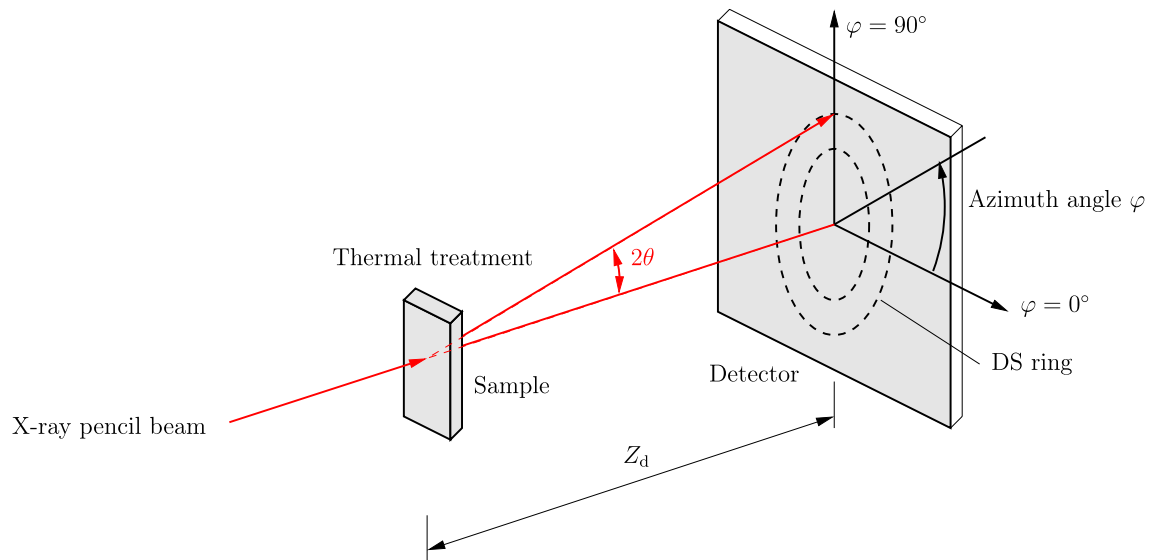
Fig. 1. Schematic drawing of diffraction geometry: X-ray pencil beam passes the sample; its axis should be identical with the detector center. The diffraction pattern is recorded by the planar pixelated detector placed at distance Z_d from the specimen.

$$\Phi = tan^{-1}\frac{Y}{X} \tag{2}$$

Regarding virtual monochromatization, we can assume that the X-ray diffraction pattern will have the same shape for each X-ray beam energy and will differ only in scale. This means that, for example, DS circle changes only in their diameter, depending on the energy of the X-ray beam. It follows that, knowing the energy and position on the detector of each photon registered, all energy-dependent diffraction patterns can be rescaled to an identical one with a suitably chosen reference energy. Thus, we can explain such a statement on the basis of a Bragg's law equation:

$$n\lambda_r = 2d \cdot sin\theta_r \tag{3}$$

$$n\lambda_a = 2d \cdot sin\theta_a \tag{4}$$

where n is the diffraction order, and λ_r is the wavelength of X-ray photons. Index r denotes its reference value, and index a denotes the actually measured wavelength. Variable d is the distance between specific lattice planes, which is the same for both wavelengths. θ_r is the diffraction angle for the reference wavelength, and θ_a is the diffraction angle for the actual photon wavelength. If reference photon energy e_r differs from actual energy e_a with ratio k, we can write:

$$k = \frac{e_a}{e_r} = \frac{\lambda_r}{\lambda_a}, \tag{5}$$

Dividing Eqs. (3) by Eq. (4), we obtain:

$$k = \frac{sin\theta_r}{sin\theta_a} \tag{6}$$

With a given distance between an object (diffracting crystal) and detector plane Z_d and measured radius r_a of the registered photon from the beam center at the detector plane (i.e. distance in the polar coordinates), we can measure the actual diffraction angle $2\theta_a$ at azimuth angle ϕ as follows:

$$2\theta_a = tan^{-1}\frac{r_a}{Z_d} \tag{7}$$

Similarly, for a photon with a reference wavelength, we can write:

$$tan2\theta_r = \frac{r_r}{Z_d}, \tag{}$$

hence

$$r_r = z_d tan2\theta_r \tag{8}$$

Diffraction angle $2\theta_a$ of the photon with measured energy e_a is related to diffraction angle θ_r of the photon with reference energy e_r by Eq. (5), i.e.:

$$\sin\theta_r = k \cdot \sin\left(\frac{1}{2}\tan^{-1}\frac{r_a}{Z_d}\right) \tag{9}$$

Now, we can express radius r_r which refers to a photon with reference energy e_r:

$$r_r = z_d \cdot \tan 2 \cdot \sin^{-1}\left(k \cdot \sin\left(\frac{1}{2}\tan^{-1}\frac{r_a}{z_d}\right)\right) \tag{10}$$

Using Eq. (10), for all photons with different energies which satisfy Bragg's law at a given lattice plane distance d, the radius r_a is recalculated to radius r_r like they have the same reference energy. All photons lay on the same reference radius r_r forming one DS circle or one diffraction peak on the 1D diffraction pattern, if the azimuthal angle is not taken into account (circular integration). Thanks to this, all photons that have passed through the sample can be used for diffraction analysis. Diffraction measurements can thus be performed quickly, with relatively good temporal resolution.

Experimental setup

The experimental setup is shown in Fig. 2. An industrial GE Isovolt 160 M2/0.4–3.0 tube (1) was used as a polychromatic X-ray source. The tube was installed together with a pencil-beam collimator (2) with a square aperture of 0.5×0.5 mm on a vertical stage (3). The pencil beam passes through the steel sample (4), which is fixed in the clamps of the thermomechanical processing simulator (5). The diffracted photons are registered by a camera equipped with a Timepix 3 detector (6), along with information about their position and energy. The Timepix 3 detector is water cooled to maintain a constant temperature of 20 °C, ensuring a stable energy response of the detector.
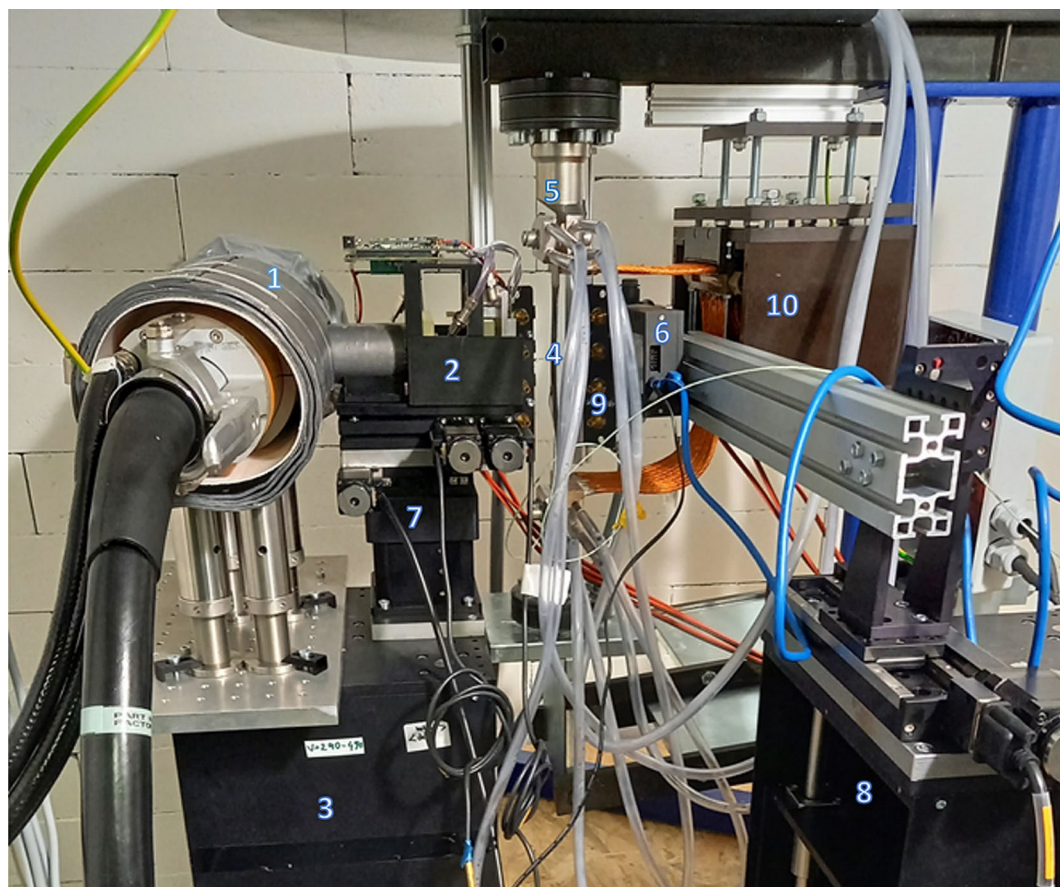

Fig. 2. Experimental setup. 1—X-ray tube, 2—pair of double slit collimator; 3—vertical stage holding collimator with positioning system; 4—specimen; 5—top grip of the simulator with water cooling; 6—Timepix 3 detector; 7—four axis positioning of the collimator; 8—vertical stage with three axis positioning of the detector; 9—jets for air cooling of the specimen; 10—resonant heating of the specimen with cables connected with the specimen.

The X-ray tube is shielded by lead of 1 cm thickness to suppress the leakage of X-rays from the tube body. The X-ray beam is pre-collimated with a lead cylinder. Then, it is collimated into a pencil-beam shape by the pair of double slits made from 9.5 mm thick lead glass, which are installed in a common frame. The resultant pencil beam has a square cross Section 0.5×0.5 mm. The position of the collimator frame is adjusted against the tube spot by the positioning stage (7), which is mounted from two rotations and two linear axes. This allows the signal registered by the detector to be maximized, i.e. the collimating slits are fully opened. Similarly, the position of the detector relative to the beam is positioned by stage (8). It has one vertical and one horizontal axis to have the pencil beam pointed at the center of the Timepix 3 detector. A beam stopper, blocking direct view of the X-ray beam, is mounted directly on the Timepix 3 detector cover window, after aligning the axis of the pencil beam to the center of the detector. All axes are driven by stepper motors, allowing positioning via computer.

A thermomechanical treatment simulator[23] is equipped with air and water moisture jets (9). These jets ensure precise control of the heat treatment profile by utilizing a dedicated PLC (not visible in Fig. 2). A temperature probe, for ensuring temperature control, is bonded onto the specimen. The specimen itself is threatened by direct ohmic heating. The heating process is controlled by a resonant frequency converter (10) with a maximum power of 9 kW at 16 kHz. The maximum heating and cooling capability is 100 °C/s. Tensile strain can be realized by the 20 kg payload at the bottom of this simulator. The operator designs a temperature profile using a spreadsheet or graphical interface, which is followed by the PLC regulator.

The Timepix 3 hybrid pixelated detector[21,24] can record time-of-arrival (ToA) and time-over-threshold (ToT) simultaneously in each pixel. The ToT mode used in this work, enabling the energy measurement of each registered photon, is used in this work. ToT has 10 bit depth with maximum event rate of 1.3 kHz per pixel (85 MHz per device). The Timepix 3 chip, containing 256×256 pixels (55×55 μm^2), has an active area of 14×14 mm and can be equipped with various sensors in terms of material and thickness. Its energy calibration is done utilizing several well defined radiation sources—XRF targets plus isotope source, see[25] for more details about this procedure. An example of the spectra of the ^{241}Am isotope source, encapsulated in stainless steel foil, measured by the Timepix 3 detector is depicted in Fig. 3. For this work, a Timepix 3 detector equipped with a 500 μm thick silicon sensor was used. This detector offers a reasonable efficiency of 1.5% for a given spectrum of X-rays passing through the sample, while offering two times better energy resolution (FWHM is typically ~ 4 keV) than a CdTe sensor (FWHM ~ 8.5 keV). Both resolutions were measured at 59.54 keV (241Am gamma source). Therefore, the Timepix 3 detector with a Si sensor was chosen for this work, even though CdTe has a much higher efficiency of 77% under the same experimental conditions. Using a CdTe sensor would have required a larger distance between the sample and the detector with respect to the readability of the diffraction patterning, hence a detector with a larger active area than it was available during this work measurement.

The Timepix 3 detector has a data-driven readout architecture that allows for a readout of each hit pixel. It can achieve a throughput of up to 38 Mhits/s by utilizing a USB 3.0-based interface, further details about the detector architecture can be found in[24]. The Timepix 3 device is controlled by the PIXet software[26]. The complete device is manufactured by Advacam Ltd., Prague, Czech Republic under the name AdvaPIX. The data is read as a continuous stream mode, where the pixel coordinates and measured energy are available for each registered photon. The continuous stream mode ensures that the probability of more than one event occurring in a particular detector pixel is negligible, contrary to the sequential (frame-based) mode. The recorded data were then processed by a specialized plug-in module that is part of PIXet software (PIXet Pro 1.8.3., https://advacam.com/camera/pixet-software/) A full-energy spectrum for each detector pixel is obtained in this way, i.e. Timepix 3 can work as an energy dispersive detector. During the experiment, the Timepix 3 detector was covered with aluminum foil to reflect the intense thermal radiation coming from the heated sample; otherwise, the detector could have been damaged. A beam stopper made of lead was installed in front of the sensor center
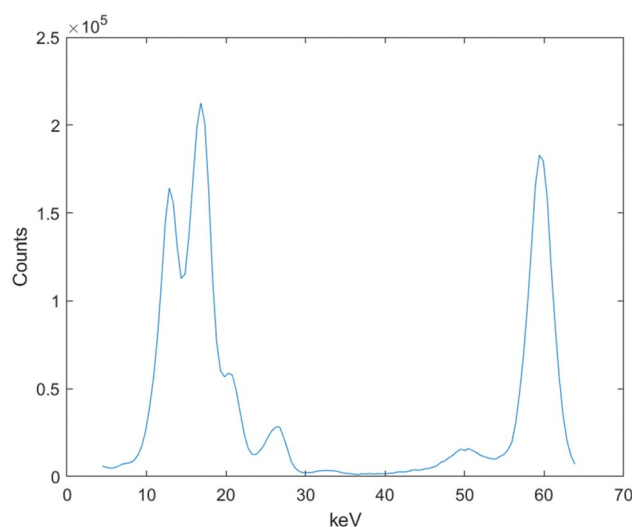

Fig. 3. Spectrum of the 241Am isotope source measured by the Timepix 3 detector with Si sensor consist from lines with energy13.95, 17.74, 20.8, 26.35 and 59.54 keV. Back scattering peak is visible at ~ 50 keV.

utilizing a plastic holder. The beam stopper holder, practically fully transparent for X-rays above 20 kV, is made of plastic utilizing a 3D printer.

Rietveld refinement adapted for the EDXR technique

For reliable identification of diffraction peaks, Rietveld refinement[22] is usually used. The Rietveld analysis is today widely used for most common X-ray diffraction powder technique. Available related analytical software, listed in[27] for instance, incorporate specific properties of the commercially available powder X-ray diffractometers. Recently, such software was utilized also for HEXRD[28,29], regardless of other physical phenomena caused by the passing of the pencil beam through the sample in contrast to the powder XRD technique. In this work, it was found that these phenomena could have quite a significant effect on the resulting XRD pattern.

For Rietveld refinement applied for transmission EDXRD, it is necessary to have relevant theoretical model of the whole setup including X-ray spectrum; detector efficiency (with dependence on photon energy); energy resolution and granularity of the detector; positions and relative intensity of the expected diffraction peaks. The theoretical broadening of diffraction peaks at a given X-ray beam spectrum is determined by the energy resolution of the detector, the properties of the X—ray pencil beam collimator, the thickness of the material under examination and the distance between the sample and the detector. The theoretical positions of the diffraction peaks were calculated using Bragg's law, and their relative intensities were taken from[30]. It should be emphasized that although the angles of photon diffraction were recalculated to obtain diffractograms as if a monochromatic X-ray source was used, other energy-dependent parameters, such as attenuation, efficiency, or peak broadening, have to be calculated for the original photon energy.

An example of a simulated X-ray spectra of an X-ray tube with a tungsten target at a voltage potential of 90 kVp is shown in Fig. 4. Energy bins were selected identical with these ones for Timepix 3 measurement. Characteristic K_α and K_β peaks of the tungsten are visible. The red curve shows the spectrum detected by a Timepix 3 detector with a 500 μm thick CdTe sensor after transmission through the 1.5 mm specimen. Although the spectrum for the Si sensor is practically identical in shape, its intensity is 50 times lower, so it is not plotted here.

Note that the emitted spectrum has almost zero intensity below 40 keV, so all photons below this value were excluded during data processing, thus significantly suppressing the effect of Compton scattering. As a consequence, the fluorescence signal emitted from the steel under investigation is not present in the resulting spectrum.

The complete physical model of the diffraction device allows to analyze the individual factors influencing the diffraction peak broadening. The resulting peak broadening is determined by the convolution of several main factors.

Energy resolution of the detector has a constant effect on the broadening of the diffraction angle. Note that, in accordance with Bragg's law (3), the spectrum of transmitted X-ray photons must be taken into account when calculating the resulting peak broadening. As a result, a larger distance leads to greater diffusion of the diffraction peaks in the detector plane caused by the detector energy resolution. The difference between the diffraction patterns for both sensors is shown in Fig. 5, for conditions including an identical object-detector distance of 37.5 mm, a collimator width of 0.5 mm, a specimen thickness of 1.5 mm, an X-ray tube voltage potential of 90 kVp, and a 0.6/0.4 mixture of α-Fe and γ-Fe fractions. Since Timepix 3 with a Si sensor has better energy resolution than a CdTe sensor, its effect on the overall FWHM is lower, although still significant.

Thickness of the transmitted specimen influences peak broadening as the photon interaction near to the surface closest to the X-ray source causes wider diffraction angle than the photon reflected in a point exiting specimen on the detector side. Peak broadening p_b width (i.e. not angular) caused by the specimen thickness t can be expressed by the following equation:
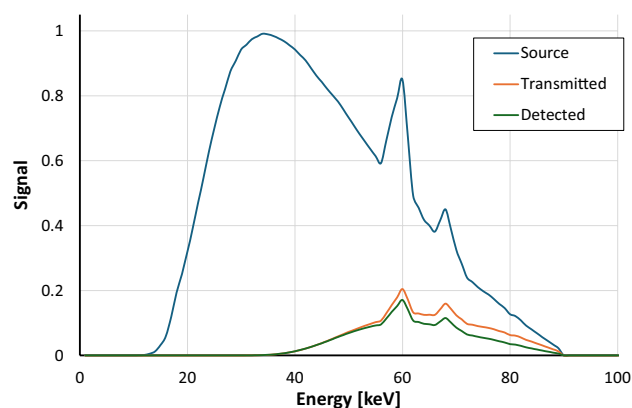
$$p_b = t \cdot \tan 2\theta_a, \tag{11}$$

Fig. 4. The simulated X-ray tube spectrum is plotted in blue. The red curve represents the spectrum after the beam passed through a 1.5 mm thick steel sample, showing negligible intensity up to 40 keV. The green curve displays the spectrum of photons detected by the CdTe Timepix 3 detector.
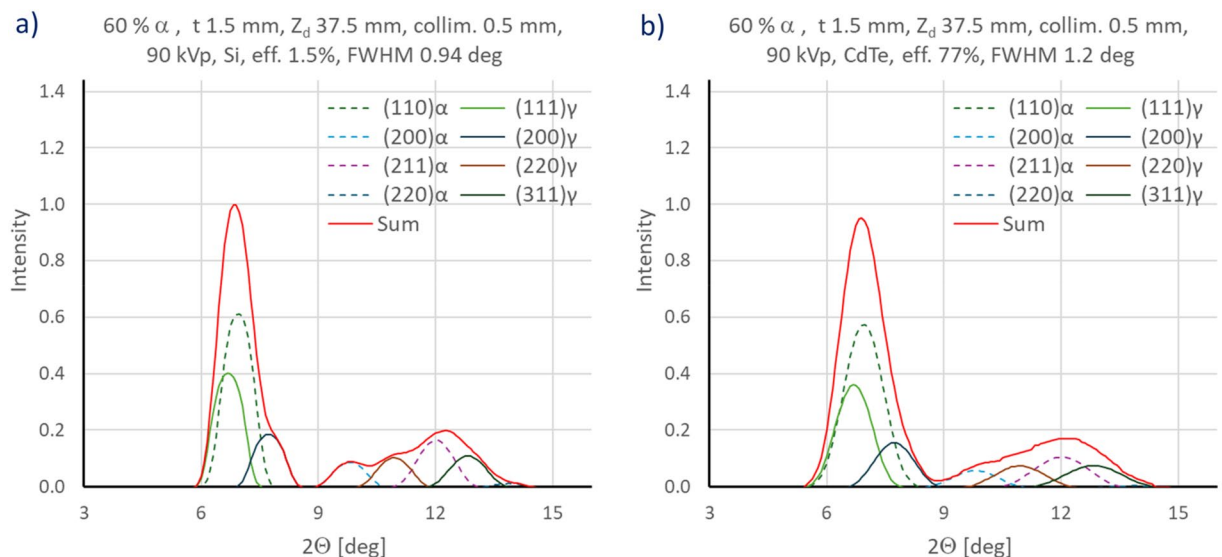
Fig. 5. Comparison of the energy resolution of Timepix 3 devices equipped with Si and CdTe sensors: (**a**) individual diffraction peaks are better separated for the Si sensor, with a total FWHM of 0.94º, which is 50% determined by the beam width, 18% by the sample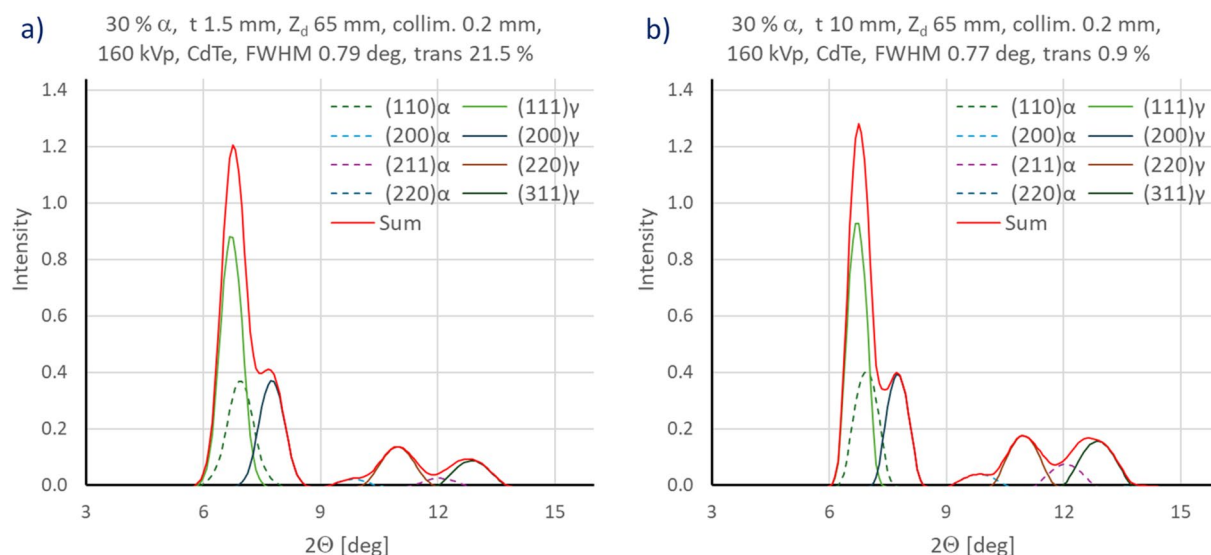 thickness, and 32% by the energy resolution of the detector; (**b**) while for the CdTe sensor with a total FWHM of 1.2º, which is 36% given by the beam width, 13% by the sample thickness, and 51% by the energy resolution of the detector.

Fig. 6. Diffraction pattern (**a**) for 1.5 mm thick sample has slightly worse FWHM, which is 13% determined by the beam width, 12% by the sample thickness, and 75% by the energy resolution of the detector; than (**b**) FWHM for 10 mm thick specimen, 8% caused by the beam width, 47% by the sample thickness and 45% by the detector.

where θ_a is the diffraction angle of a photon with energy e_a. A thicker specimen generally causes a broader diffraction peak, an effect that decreases as the energy of the incident photon increases. In addition, with a polychromatic X-ray source and the well-known beam hardening effect (i.e., softer photons are attenuated more readily), a thicker specimen leads to a lower fraction of photons with larger diffraction angles. Consequently, the angular peak broadening can be lower for a thick specimen than for a thin one, as documented in Fig. 6. This is shown by comparing case a), with a specimen thickness of 1.5 mm, and case b), with a specimen thickness of 10 mm.

Both cases were simulated for an object-detector distance of 65 mm, a collimator width of 0.2 mm, an X-ray tube voltage potential of 160 kVp, and a 0.3/0.7 mixture of α-Fe and γ-Fe fractions. Note that although the thicker specimen exhibits a lower total FWHM, it attenuated X-rays 24 times more than the thin one.

The diameter of the pencil beam has a similar effect to the thickness of the sample. A larger diameter causes a wider diffraction peak and vice versa. On the other hand, a smaller beam diameter provides a lower intensity of the resulting beam. Similar to the effect of sample thickness, this source of beam broadening is not angular if the beam divergence is negligible compared to the distance of the sample from the detector (as is usually required). As a result, the relative contribution of the pencil beam profile to the total FWHM decreases with increasing distance of the sample from the detector. Note that although the pencil beam trace is ideally trapezoidal in shape, in reality it is square with exponential wings—this factor is another parameter that can be taken into account in Rietveld analysis.

Increasing the distance between the sample and the detector improves the recognisability of individual peaks in the diffraction pattern. This effect is shown by comparing Fig. 5 with Fig. 7, where the behaviour of both the Si and CdTe sensors is demonstrated. For the data in Fig. 7, an object-detector distance of 100 mm, a collimator width of 0.2 mm, an X-ray tube voltage potential of 160 kVp, and a 0.5/0.5 mixture of α-Fe and γ-Fe fractions were used.

Although increasing the distance between the sample and the detector helps, it must be taken into account that its maximum value is limited by the size of the active area of the detector used, so the distance was set to 37.5 mm. Similarly, due to the properties of the collimator (limited X-ray attenuation ability) the tube voltage was limited to 90 kVp.

Measurement

The specimen of low-alloy nickel–chromium steel containing 0.4% carbon had the shape of a strip 50 mm wide and 1.5 mm thick, which was fixed in the thermomechanical processing simulator. The heat was linearly raised 7.5 K/s up to 750 °C of the austenitic transformation, 100 s after beginning the experiment. Quenching in air was realized at two steps—the bainitic (200–300 s) at 450 °C and martensitic transition (500–600 s) at 200 °C with cooling of 3 K/s. The maximal error was at ambient temperature (18.1 °C). The error is in the tolerance band of ± 5 °C. Whole temperature diagram is plotted in Fig. 8, where the power consumption of the thermomechanical treatment simulator is shown as well. It can be seen that the peaks in energy consumption are related to phase transitions—especially during cooling. Due to the energy consumed by recrystallization between 200 and 240 s, the thermal energy input required to maintain the prescribed temperature profile increased significantly.

During diffraction measurement, the GE Isovolt X-ray tube was operated at 90 kV and 7 mA in the small focal spot mode, having a spot size of 1 mm. The cross section of the pencil-beam aperture was 5× smaller than the tube spot size; therefore, 80% of the photons didn't pass through the collimator. Note that the large focus mode of the X-ray tube, allowing a higher tube current, leads to a lower photon emission density on the target, while the effective pencil-beam intensity is then practically the same. It was not possible to use higher voltage, because it caused too intense scattering on the beam stopper which was used.

During 700 s of thermal processing of the sample, a total of 1.5 million photons were detected by the Timepix 3 detector, which is three orders of magnitude less than the capability of the Timepix 3. The collimator-sample-detector distances was set on 37.5 mm, which ensures that the expected DS rings remain inside the active area of the detector, which in our case is relatively small (14×14 mm).
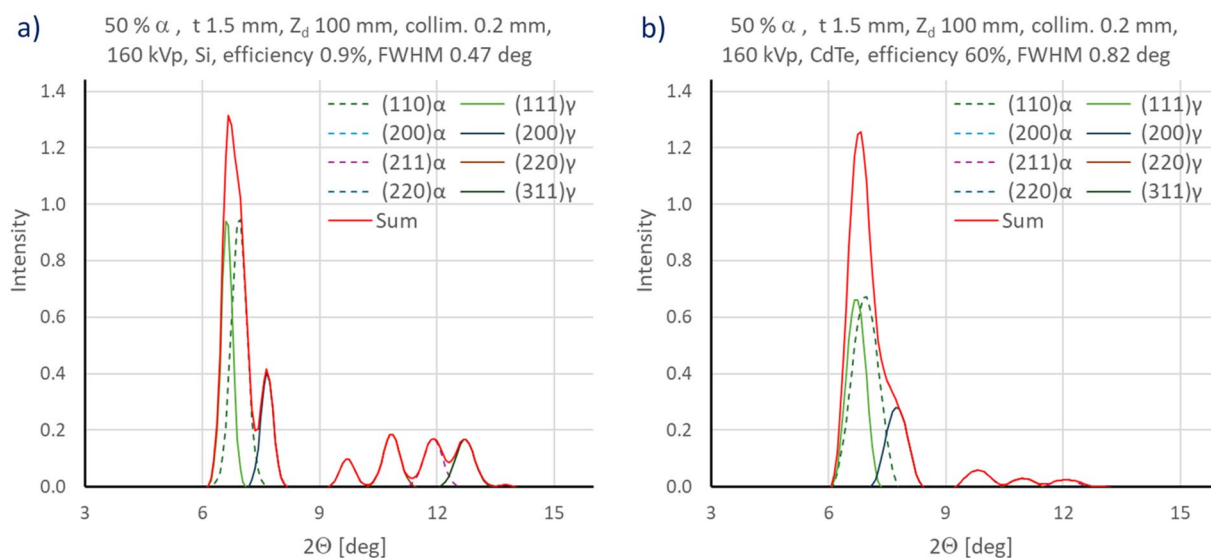

Fig. 7. Increasing the distance between the sample and the detector improves the identification of diffraction peaks. For the Si sensor, the diffraction pattern's FWHM is almost two times lower than that of the CdTe sensor. The contribution of the detector's energy resolution to the total FWHM is 70% for the Si sensor and 82% for the CdTe sensor.
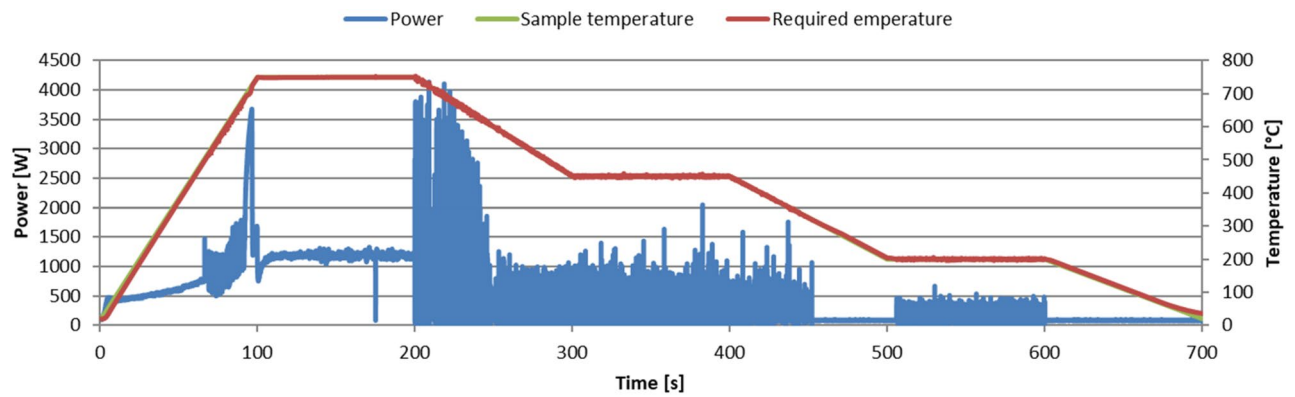
Fig. 8. Temperature diagram along with simulator power consumption. The peak energy consumption shows the start of austenitisation at 90 s. Cooling started at 200 s. This was followed by bainitic transformation in the time interval 300–400 s and martensitic transformation in the interval 500–600 s.
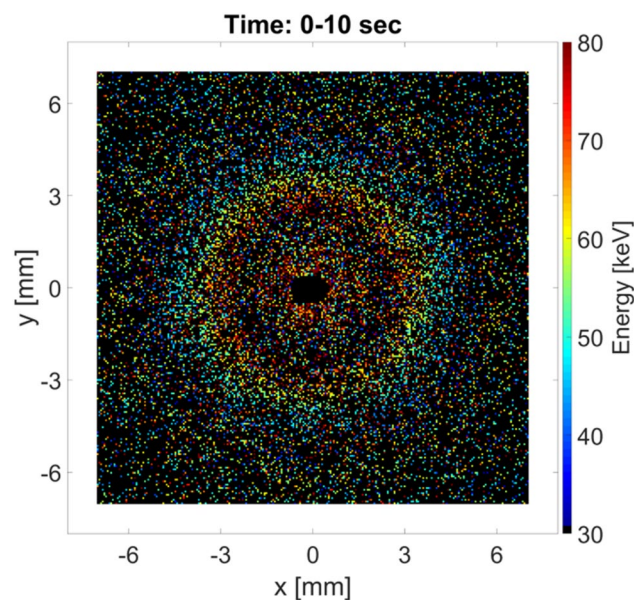

Fig. 9. Polychromatic diffraction image taken during the first 10 s. The colors correspond to the energy of the recorded photons.

Experimental data processing and diffraction pattern analysis
Correction of the pencil beam position

Concerning data processing, the photons acquired by the Timepix 3 detector were sorted by energy into 1 keV bins. To obtain reasonable data statistics, these data were processed with 10 s' integration time, i.e. a total of 70 data sets were analyzed to show the time evolution of the steel-lattice parameters. An example of the image, where the energy of each photon is shown in color representation, is depicted in Fig. 9. The data recorded during first 10 s are visualized below. Coordinate [0,0] corresponds to the axis of the pencil beam. The data behind the beam stopper were masked for a better clarity. It is clearly visible that higher energies are closer to the image center and that lower energy photons are farther out, respectively. For illustration, such an image obtained over a time period of 190–200 s, is depicted in Fig. 10. It is visible that the second image is different from the previous image.

Polychromatic diffraction data were transformed into virtually monochromatic diffraction patterns for the whole heating profile with a time step of 10 s according to Eq. (10), where reference value 50 k eV was chosen. As mentioned above, the data were sorted with an energy bin equal to 1 keV. To avoid ambiguity, events where more than one photon was count in one particular pixel were excluded during monochromatization for each energy bin. This situation occurred mainly in the area influenced by the scattering caused by the beam stopper. The Cartesian coordinates of the detector pixels were of course first transformed to polar coordinates utilizing Eqs. (1) and (2). An example of such processed data is depicted in Fig. 11, which corresponds to the end of the experiment. The vertical axis has the meaning of the radial distance of a particular pixel from the center of the
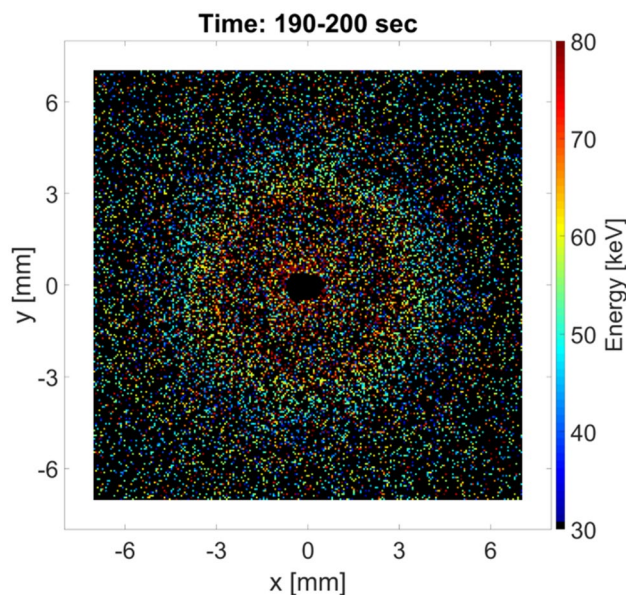
Fig. 10. Polychromatic diffraction pattern recorded at the end of the austenitization temperature.
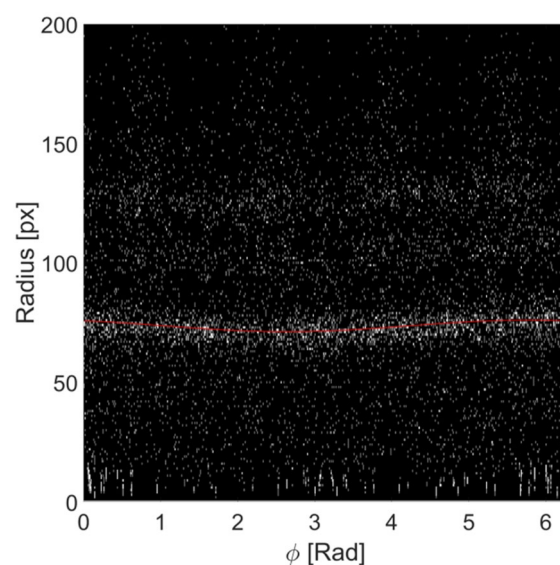

Fig. 11. Diffraction data from the time period 690–700 s, recalculated into equivalent energy of 50 kV, polar coordinates. Pencil-beam position is not corrected.

detector (for it is equal to zero), the maximum radius corresponds to one-half of the detector diagonal. The horizontal axis represents the azimuthal angle (see Fig. 1). The first peak, marked by the red line, corresponds to diffraction plane (110)α; however, in polar coordinates, it should have the form of a straight line, except for the deformed material (not in our case). The reason for such a situation is misalignment of the pencil-beam axis and the detector center at the beginning of the measurement. This results in consequent drifting of the X-ray tube focal spot, which is expected for the industrial tube type used. Correction of the beam axis position was done by numerical minimization of amplitudes b and c of the fitting function:

$$f_{a \to 0, b \to 0} = a + b \cdot sin\left(\varphi - \varphi_0\right) + c \cdot cos\left(\varphi - \varphi_0\right) \tag{12}$$

Variable a denotes the position of the first diffraction peak, φ is the azimuth angle, and φ_0 is the angle shift. Note that amplitude values b and c are changing varying differences [dx, dy] in Eq. (1). These amplitudes are zero, if the position of the beam axis is correctly determined and the sample is not strained. It was found that the beam axis misalignment at the beginning was 0.075 mm. This misalignment grew up to the maximal value at the end of the experiment, where it reached 0.14 mm (2.5 pixels). In addition, it was found that detected amplitudes b
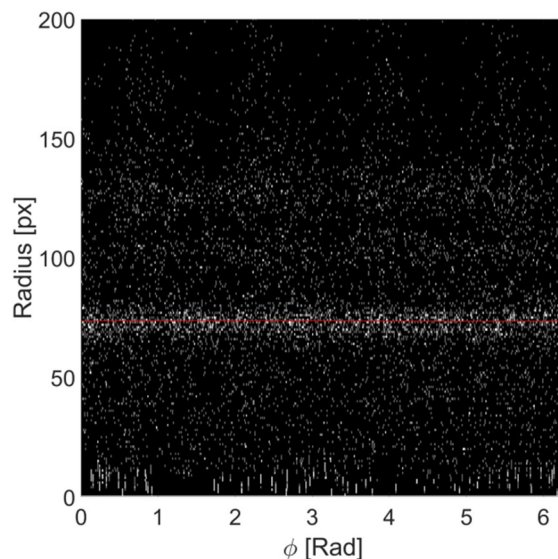
Fig. 12. Diffraction data from the time period 690–700 s. Pencil-beam position is corrected. Almost all dots represent a single event (during 10 s).
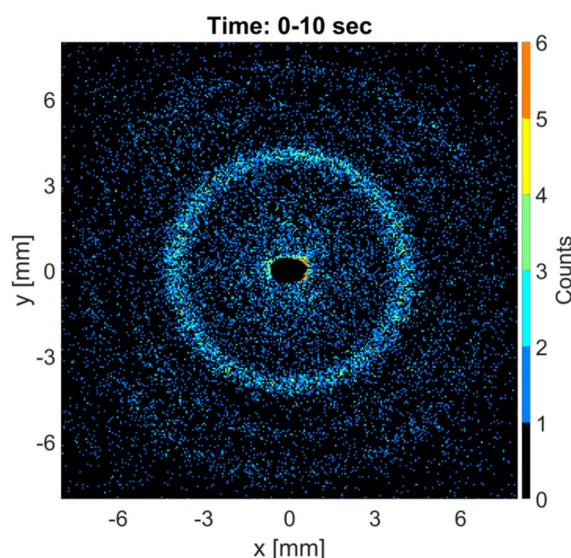

Fig. 13. Monochromatized diffraction pattern from the time period 0–10 s, recalculated into equivalent energy of 50 kV, Cartesian coordinates.

and c are almost equal to zero; more precisely, their values are at the noise level. Therefore, a detector with a higher resolution would be needed to measure the possibly existing very small deformation. The diffraction image obtained using this correction is depicted in Fig. 12. As mentioned above, a total of 70 diffraction patterns, obtained within a time period of 10 s, were processed. This includes a correction for pencil-beam position drift. For additional analysis, these patterns were summed along the azimuth angle, i.e. circular integration was done in this way, and a 1D diffraction pattern was obtained.

2D diffraction pattern after virtual monochromatization
The monochromatic diffraction pattern can of course be converted from polar to Cartesian coordinates to show clearly visible DS rings. A XRD pattern related to the first ten seconds is shown in Fig. 13; compare it with Fig. 9, where the same data are shown before monochromatization. Note that number of monochromatized photons was practically the same as before monochromatization. Although the statistics of the data is rather low, DB rings corresponding to the diffraction planes (110)α, (200)α and (211)α can be identified. In this case, the circles could be fit quite reliably and thus their diameters could be found. Note that the area beyond the detector has visualized some photons with lower energy and that these have a large diffraction angle after

monochromatization. A pattern relating to the onset of the end of the austenitization temperature is shown in Fig. 14. The maximum peak is clearly visible, while the others are indistinct. In addition, it will be shown in the next section that a mixture of α-Fe and γ-Fe fractions are present in this state that cannot be directly identified in this 2D representation. However, it will be shown that these fractions can be resolved in a 1D representation of the diffraction data using Rietveld analysis.

1D diffraction pattern after virtual monochromatization and Rietveld analysis

Circular integration (i.e., summation of diffraction data in polar coordinates over the azimuthal angle) of the monochromatic diffraction pattern was performed at seventy 10-s intervals. The resultant time evolution of the 1D diffraction pattern is shown in Fig. 15. For the situation when the detected photons were outside the circle enclosed by the detector area, the signal was normalized by the whole length of the circle divided by the part of the circle lying in the detector area. The data smoothing (a floating average of 4×4 pixels) was done to suppress noise for this visualization, in addition, the background caused mainly by the Compton scattering was removed. As expected, a significant change of the scattering pattern is visible around the time period of the austenitization temperature. The relation between time and temperature is depicted in Fig. 8.

For an analysis of the thermal treatment of the steel, a 1D diffraction pattern was analyzed by the Rietveld refinement for each time step. Note that for Rietveld refinement, data without this smoothing with removed background was used to preserve temporal resolution. The measured 1D diffraction patterns from the six selected states, together with the results of the Rietveld refinement analysis, are shown in Fig. 16. For the first state at 10 s form the experiment beginning, the first peak corresponds to (110)α, the second to (200)α, the third to (211) α and fourth to (220)α. For the condition at 100 s, austenitization process already led to the 41% of the γ-Fe. For the last 200 s condition, when the temperature was maintained at austenitizing, α-Fe was still present; the austenitisation process was not fully completed. The next state at the 250th second corresponds to the moment when the power supplied by the treatment simulator dropped significantly, austenite was still present in the steel. The following state in the 300th second corresponds to the beginning of the bainitic transformation. In the last depicted state at the 500th second, only α-Fe is present again.

The evolution of the α-Fe/γ-Fe fraction ratio is shown in Fig. 17. It shows that the onset of austenitizing transformation was relatively slow. This transformation, once the austenitisation temperature was fully reached, proceeded relatively slowly and was not fully completed within 200 s. The exponential fit of the austenitization process indicated that approximately three times longer time would be required to complete the transformation.

Discussion

The analyzed diffraction peaks were quite broad, important factors influencing diffraction peak blurring was the relatively high ratio between the pencil-beam diameter and the distance between the sample and the detector with respect to sample thickness. The short distance between the detector and the sample also made it difficult to separate peaks that have a small difference in diffraction angles. However, this problem was successfully solved by Rietveld refinement considering all the parameters of the diffraction setup.

For further experimental work, a Timepix 3 detector with a cadmium telluride sensor will be used. This sensor has 50 times better efficiency than the silicon sensor detector used in this work under the same experimental conditions. In addition, the newly available MetalJet D2 + 160 kV X-ray tube has a focal size of only 20×20 μm at 250W. Therefore, it will be possible to use a much smaller diameter pencil beam, which will improve the quality of diffraction pattern imaging. Likewise, the photon fluence will not be reduced by the pencil-beam aperture, resulting in a further fivefold increase in signal. Thus, a total of 250 times better temporal resolution can be
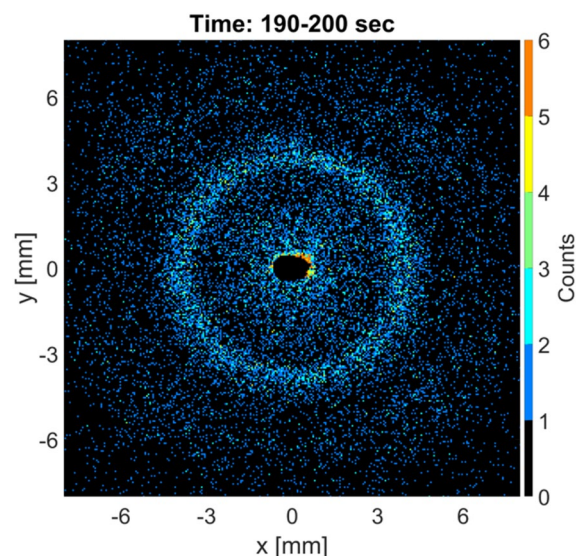

Fig. 14. Monochromatized diffraction pattern from the time period 190–200 s.
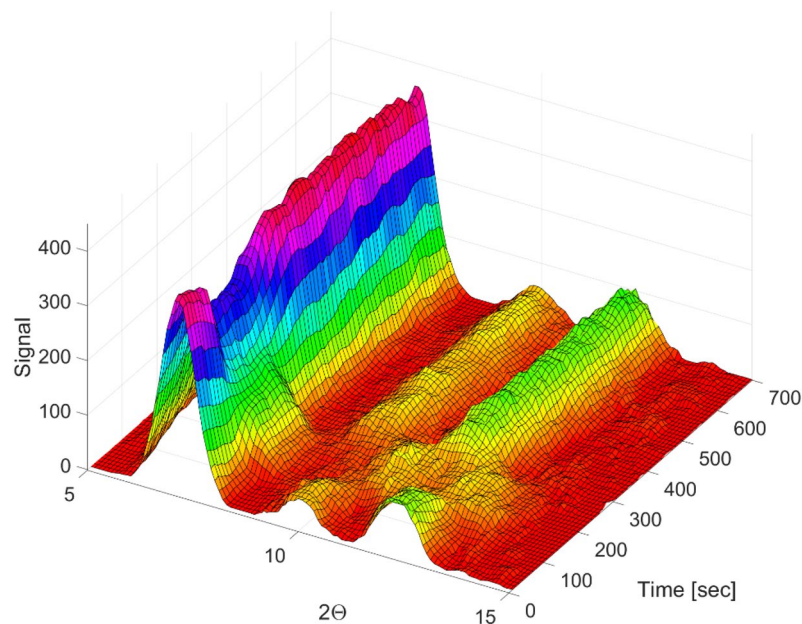
Fig. 15. Time evolution of the 1D monochromatized diffraction pattern plotted using Matlab software (version R2019a, MathWorks®, USA). For example, the maximum peak on the left corresponds to (110)α during the first time period of 10 s. The first change in the diffraction pattern is clearly visible at 100 s, where austenitization is already pronounced, while the diffraction pattern returns to the initial state of the steel at 250 s.
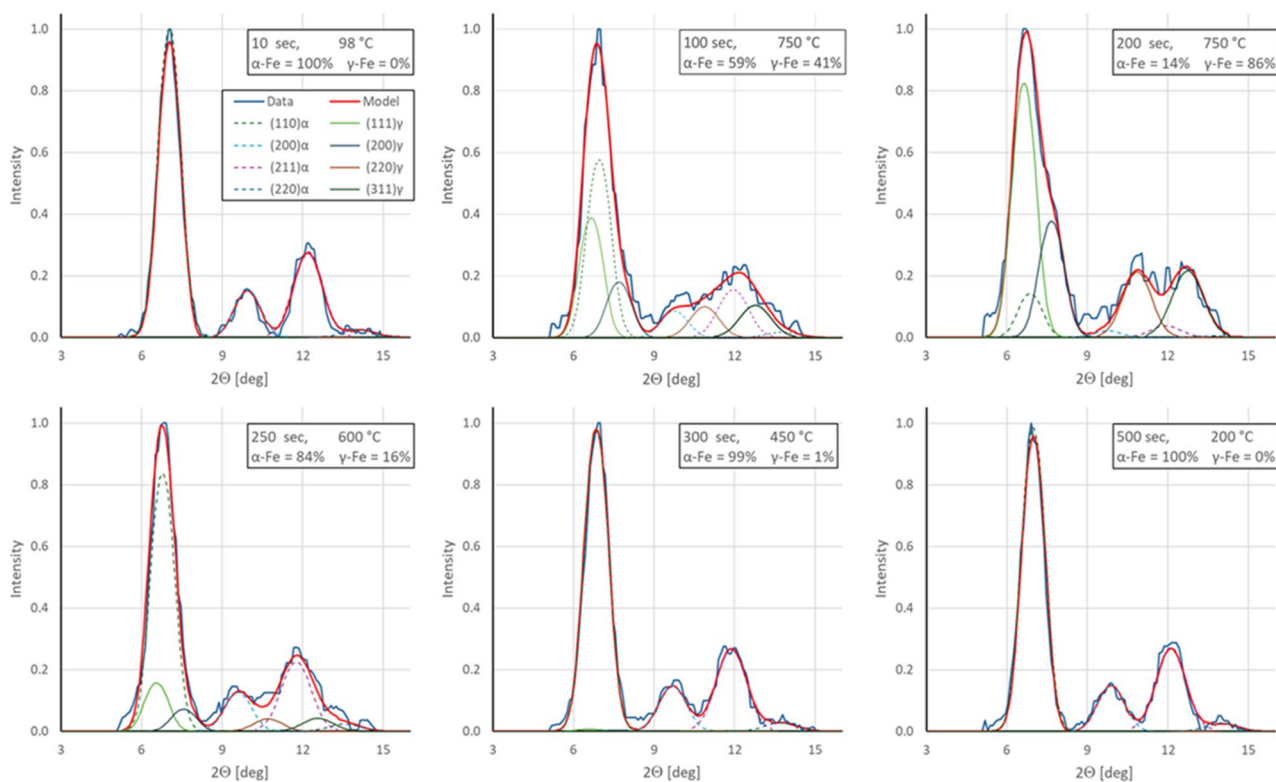

Fig. 16. Selected states of the of the 1D diffraction pattern evolution. For each state, the time from the beginning, the actual specimen temperature, and the α-Fe / γ-Fe fractions are depicted in a box at the top.

Fig. 17. Time evolution of the α-Fe and γ-Fe fractions. Austenitisation began at 90 s from the start of the experiment, the γ-Fe fraction is larger than α-Fe from 110 s, but this transformation is not fully completed until the onset of cooling.

expected. At the same time, a detector with 4 times more area will be used. This will allow the distance between the detector and the sample to be increased, improving the separation of peaks with close diffraction angles.

Improved separation of diffraction peaks can be achieved by increasing the active area of the detector while extending the distance between the sample and the detector. For this reason, a new Timepix 3 detector will be built, consisting of four individual chips. This will have a hole in the middle to allow the pencil beam to pass freely through it.

The next experiments are planned with a focus on precise knowledge of the steel structure and phase transition times. Accordingly, the temperature–time profile should be set with a detailed knowledge of the ongoing steel processes. We plan to use AI for the cooling process design[1].

Conclusions

It has been shown that energy dispersive X-ray diffraction (EDXRD) can be used to analyze the austenitic phase transition under laboratory conditions with an excellent temporal resolution of ten seconds, which is partially comparable to the resolution of synchrotron setups. The EDXRD method can of course be used not only for steel, but also for the observation of fast physical processes in any other metallic or non-metallic crystalline material.

EDCRD works with virtual monochromatization of the polychromatic diffractogram. Thus, the full spectrum of a powerful industrial X-ray tube can be used to obtain an intense diffraction signal. As has been demonstrated, the inevitable fluctuations in the spot position of the industrial X-ray tube, which affect the quality of the diffractogram, can be successfully corrected in the data processing stage.

While the polychromatic X-ray beam used is intense, the effective energy it uses for transmission diffraction is high enough to penetrate even relatively massive objects. This significantly extends the possibilities of diffraction techniques, even for the routine analysis of objects with real dimensions.

The thermomechanical simulator showed excellent performance in terms of agreement between the desired and achieved temperature profiles of the heat treatment. Changes in the power supplied by the simulator to the sample to maintain this profile indicate the start and end of the austenitization transition. This agrees well with the phase changes detected by the EDXRD method.

Further improvement in the temporal resolution of the presented EDXRD method can be achieved by using the CdTe sensor material of the Timepix 3 energy dispersive detector. As a result, in conjunction with the newly available MetalJet X-ray tube which has a smaller spot with a higher emission density than tube used in this work, 250 times better temporal resolution can be expected. This is less than 0.05 s for the same thickness of steel sample used in this work.

Data availability

Polychromatic high-energy X-ray diffraction data recorded with the Timepix energy dispersive detector and monochromatized data calculated on the basis of knowledge of the energy of each registered photon and the geometry of the X-ray diffraction experiment have been deposited in the repository of the Czech Academy of Sciences. All data stored in Matlab format are available at [https://doi.org/10.57680/asep.0599412] (https:/doi.org/https://doi.org/10.57680/asep.0599412).

References

1. Khalaj, O., Hassas, P., Masek, B., Stadler, C. & Svoboda, J. Optimization of cooling rate of Q-P treated 42SiCr steel using AI digital twinning. *Helion* **10**, e32101. https://doi.org/10.1016/j.heliyon.2024.e32101 (2024).

2. Speer, J., Matlock, D. K., De Cooman, B. C. & Schroth, J. G. Carbon partitioning into austenite after martensite transformation. *Acta Materialia* **51**, 2611–2622. https://doi.org/10.1016/S1359-6454(03)00059-4 (2003).
3. Esin, V. A. et al. In situ synchrotron X-ray diffraction and dilatometric study of austenite formation in a multi-component steel: Influence of initial microstructure and heating rate. *Acta Materialia* **8**, 118–131. https://doi.org/10.1016/j.actamat.2014.07.042 (2014).
4. Kohne, T. et al. Evolution of martensite tetragonality in high-carbon steels revealed by in situ high-energy X-ray diffraction. *Metall. Mater. Trans. A* **54**, 1083–1100. https://doi.org/10.1007/s11661-022-06948-z (2023).
5. Sun, D. et al. In-situ observation of phase transformation during heat treatment process of high-carbon bainitic bearing steel. *J. Market. Res.* **19**, 3713–3723. https://doi.org/10.1016/j.jmrt.2022.06.112 (2022).
6. Moreno, M. et al. Real-time investigation of recovery, recrystallization and austenite transformation during annealing of a cold-rolled steel using high energy X-ray diffraction (HEXRD). *Metals* **9**, 8. https://doi.org/10.3390/met9010008 (2019).
7. Huyghe, P., Caruso, M., Collet, J.-L., Dépinoy, S. & Godet, S. Into the quenching & partitioning of a 0.2C steel: An in-situ synchrotron study. *Mater. Sci. Eng. A* **743**, 175–184. https://doi.org/10.1016/j.msea.2018.11.065 (2019).
8. Meng, Q. et al. In situ synchrotron X-ray diffraction investigations of the nonlinear deformation behavior of a low modulus β-type Ti36Nb5Zr alloy. *Metals.* **10**(12), 1619. https://doi.org/10.3390/met10121619 (2020).
9. Mo, K., Tung, H., Chen, X., Chen, W., Hansen, J. B., Stubbins, J. F., Li, M., & Almer, J. Synchrotron Radiation Study on Alloy 617 and Alloy 230 for VHTR Application. In: Proceedings of the ASME 2011 Pressure Vessels and Piping Conference. Volume 6: Materials and Fabrication, Parts A and B. Baltimore, Maryland, USA. July 17–21, 2011. pp. 759–766. ASME. https://doi.org/10.1115/PVP2011-57393
10. Bauer, S., Rodrigues, A. & Baumbach, T. Real time in situ x-ray diffraction study of the crystalline structure modification of Ba0.5Sr0.5TiO$_3$ during the post-annealing. *Sci. Rep.* **8**, 11969. https://doi.org/10.1038/s41598-018-30392-y (2018).
11. Bernier, J., Suter, R., Rollett, A. & Almer, J. High-energy X-ray diffraction microscopy in materials science. *Annu. Rev. Mater. Res.* **50**(1), 395–436. https://doi.org/10.1146/annurev-matsci-070616-124125 (2020).
12. Gesswein, H., Stuble, P., Weber, D., Binder, J. R. & Monig, R. A multipurpose laboratory diffractometer for operando powder X-ray diffraction investigations of energy materials *J. Appl. Cryst.* **55**, 503–514. https://doi.org/10.1107/S1600576722003089 (2022).
13. Kämpfe, B., Luczak, F. & Michel, B. Energy dispersive X-ray diffraction. *Part. Part. Syst. Charact.* **22**, 391–396. https://doi.org/10.1002/ppsc.200501007 (2005).
14. Gerndt, E. et al. Application of Si-strip technology to X-ray diffraction instrumentation. *Nuclear Instrum. Methods Phys. Res. Sect. A Accel. Spectrom. Detect. Assoc. Equip.* **624**, 350–359. https://doi.org/10.1016/j.nima.2010.05.032 (2010).
15. Send, S. et al. Analysis of polycrystallinity in hen egg-white lysozyme using a pnCCD. *J. Appl. Cryst.* **45**, 517–522. https://doi.org/10.1107/S0021889812015038 (2012).
16. Send, S. et al. Application of a pnCCD for energy-dispersive Laue diffraction with ultra-hard X-rays. *J. Appl. Cryst.* **49**, 222–233. https://doi.org/10.1107/S1600576715023997 (2016).
17. Abboud, A. et al. A new method for polychromatic X-ray μLaue diffraction on a Cu pillar using an energy-dispersive pn-junction charge-coupled device. *Rev. Sci. Instrum.* **85**(11), 113901. https://doi.org/10.1063/1.4900482 (2014).
18. Abboud, A. et al. Single-shot full strain tensor determination with microbeam X-ray Laue diffraction and a two-dimensional energy-dispersive detector. *J. Appl. Cryst.* **50**, 901–908. https://doi.org/10.1107/S1600576717005581 (2017).
19. O'Flynn, D. et al. Materials identification using a small-scale pixelated x-ray diffraction system. *J. Phys. D Appl. Phys.* **49**, 175304. https://doi.org/10.1088/0022-3727/49/17/175304 (2016).
20. O'Flynn, D. et al. Energy-windowed, pixellated X-ray diffraction using the Pixirad CdTe detector. *J. Instrum.* https://doi.org/10.1088/1748-0221/12/01/P01004 (2017).
21. Frojdh, E. et al. Timepix3: first measurements and characterization of a hybrid-pixel detector working in event driven mode. *J. Instrum.* https://doi.org/10.1088/1748-0221/10/01/C01039 (2015).
22. Rietveld, H. M. A profile refinement method for nuclear and magnetic structures. *J. Appl. Crystallogr.* **2**, 65–71. https://doi.org/10.1107/S0021889869006558 (1969).
23. Jirková, H., Kučerová, L. & Mašek, B. Effect of quenching and partitioning temperatures in the Q-P process on the properties of AHSS with various amounts of manganese and silicon. *Mater. Sci. Forum.* **706–709**, 2734–2739. https://doi.org/10.4028/www.scientific.net/MSF.706-709.2734 (2012).
24. Wong, W. S. et al. Introducing Timepix2, a frame-based pixel detector readout ASIC measuring energy deposition and arrival time. *Radiat. Meas.* **131**, 106230. https://doi.org/10.1016/j.radmeas.2019.106230 (2019).
25. Jakubek, J. Precise energy calibration of pixel detector working in time-over-threshold mode. *Nuclear Instrum. Methods Phys. Res. Sect. A Accel. Spectrom. Detect. Assoc. Equip.* **633**, S262–S266. https://doi.org/10.1016/j.nima.2010.06.183 (2011).
26. Turecek, D. and Jakubek, J. PIXET Software package tool for control, readout and online display of pixel detectors Medipix/Timepix, Advacam, Prague
27. Inventory of data reduction and analysis software used in high-energy X-ray research at PETRA III, TRITA-ITM-RP 2022:2. 2022. ISBN 978-91-8040-319-1
28. Bénéteau, A., Weisbecker, P., Geandier, G., Aeby-Gautier, E. & Appolaire, B. Austenitization and precipitate dissolution in high nitrogen steels: an in situ high temperature X-ray synchrotron diffraction analysis using the Rietveld method. *Mater. Sci. Eng. A* **393**, 63–70. https://doi.org/10.1016/j.msea.2004.09.054 (2005).
29. Macchi, J. et al. Dislocation densities in a low-carbon steel during martensite transformation determined by in situ high energy X-Ray diffraction. *Mater. Sci. Eng. A* **800**, 140249. https://doi.org/10.1016/j.msea.2020.140249 (2021).
30. Cullity, B. D. & Stock, S. R. *Elements of X-ray diffraction* (Pearson education, London, 2013).

Acknowledgements

Author contributions

Daniel Vavrik proposed the arrangement of the whole experimental setup, implemented the EDXRD method for data processing and wrote the main part of the text. Vjaceslav Georgiev operated the thermomechanical treatment simulator. Jan Jakubek developed and implemented the EDXRD method and Rietveld refinement for transmission XRD. Jan Sleichrt conducted the design and installation of the experimental setup positioning system. Bohuslav Masek proposed the concept of simulator. Ondrej Urban programmed routines for the thermomechanical treatment simulator. Daniel Kytyr worked on the design and installation of the experimental setup positioning system.

Declarations

Competing interests
The authors declare no competing interests.

Additional information
Correspondence and requests for materials should be addressed to D.V.

Reprints and permissions information is available at www.nature.com/reprints.

Publisher's note Springer Nature remains neutral with regard to jurisdictional claims in published maps and institutional affiliations.